Research Article Vol. 62, No. 9 / 20 March 2023 / Applied Optics 2317

applied optics

Thin flexible multi-octave metamaterial absorber for millimeter wavelengths

Giampaolo Pisano,[1,2,*] Christopher Dunscombe,[2] Peter Hargrave,[2] Alexey Shitvov,[3] and Carole Tucker[2]

[1]Dipartimento di Fisica, Sapienza University of Rome, Rome, Italy
[2]School of Physics and Astronomy, Cardiff University, CF24 3AA Cardiff, UK
[3]School of Physics and Astronomy, University College London, WC1E 6BT London, UK
*giampaolo.pisano@uniroma1.it

Received 24 October 2022; revised 6 January 2023; accepted 31 January 2023; posted 1 February 2023; published 20 March 2023

The development of radiation-absorbent materials and devices for millimeter and submillimeter astronomy instruments is a research area of significant interest that has substantial engineering challenges. Alongside a low-profile structure and ultra-wideband performance in a wide range of angles of incidence, advanced absorbers in cosmic microwave background (CMB) instruments are aimed at reducing optical systematics, notably instrument polarization, far beyond previously achievable specifications. This paper presents a metamaterial-inspired flat conformable absorber design operating in a wide frequency range of 80–400 GHz. The structure comprises a combination of subwavelength metal-mesh capacitive and inductive grids and dielectric layers, using the magnetic mirror concept for a large bandwidth. The overall stack thickness is a quarter of the longest operating wavelength and is close to the theoretical limit stipulated by Rozanov's criterion. The test device is designed to operate at a 22.5° incidence. The iterative numerical-experimental design procedure of the new metamaterial absorber is discussed in detail, as well as the practical challenges of its manufacture. A well-established mesh-filter fabrication process has been successfully employed for prototype fabrication, which ensures cryogenic operation of the hot-pressed quasi-optical devices. The final prototype, extensively tested in quasi-optical testbeds using a Fourier transform spectrometer and a vector network analyzer, demonstrated performance closely matching the finite-element analysis simulations; that is, greater than 99% absorbance for both polarizations, with only a 0.2% difference, across the frequency band of 80-400 GHz. The angular stability for up to ±10° has been confirmed by simulations. To the best of our knowledge, this is the first successful implementation of a low-profile, ultra-wideband metamaterial absorber for this frequency range and operating conditions.

https://doi.org/10.1364/AO.478842

1. INTRODUCTION

The rapid development of millimeter-wave astronomy instrumentation is partly driven by the scientific opportunity provided by cosmic microwave background (CMB) observations. In particular, ongoing CMB polarization measurements demand unprecedented instrument sensitivity and bandwidth. Proposed millimeter-wave astronomy telescopes feature large multichroic detector arrays operated at sub-Kelvin temperatures. High polarization sensitivity can be achieved with the aid of a rotating half-wave plate. The corresponding cold optics are designed for a maximum optical throughput, a wide field of view, and multiple frequency bands. As the cold detector sensitivity approaches theoretical limits and atmospheric systematics become less of an issue for space-borne instruments, low-level instrument systematics have emerged as a crucial requirement for CMB telescopes. These include instrument polarization effects, notably those associated with the rotating half-wave plate, beam fidelity, and wavefront impairments caused by stray light channeled by spurious reflections along the optical chain. In relation to stray light, there is an ongoing effort to design new absorber material for the optical cavities of the LiteBIRD telescopes [1], which will be deployed in space at the end of the 2020s to carry out an ambitious mission to detect primordial gravitational waves through observations of the CMB B-mode pattern.

Millimeter-wave and infrared absorbers are routinely used in CMB instrument design [2] to prevent reflection from the walls and surfaces of the cryostat, pupils, and baffles, as well as other structural elements along the optical path, thus terminating the stray light at the higher temperatures before it reaches the focal plane. Absorbers are designed to meet a range of interrelated,

and often conflicting, optical, structural, and thermal requirements, including low reflectivity, wide bandwidth, angular and polarization independence, small thickness, high mechanical strength, high thermal conductivity at cryogenic temperatures, practical conformability, low weight, and low cost.

Conventional millimeter-wave telescope absorbers include open foam materials loaded with carbon or stainless-steel particles [3]. Tessellated terahertz radiation absorptive material (RAM), developed by Thomas Keating Ltd. [4], is a carbon-loaded polypropylene compound manufactured by injection molding. It features a pyramidal anti-reflection structure on the exterior face and provides low reflectance in the 50–1000 GHz frequency range in a wide range of angles of incidence. However, this material is stiff, thick, and heavy, which makes it inconvenient for covering large conformal surfaces inside cylindrical optical cryostats. A modification of such RAM has been reported in [2].

Two-component conductively loaded epoxies, such as thermally conductive epoxy encapsulant Stycast 2850FT by Henkel Corp. [5], are also commonly used as submillimeter-wave absorbers in low-temperature applications [6]. A coat of Stycast2850FT usually exhibits ∼15% reflectivity, depending on the surface roughness. Epoxy coating can be molded to reduce reflectivity at lower frequencies, but the process becomes costly. A graphite-loaded epoxy-based molded pyramidal absorber, constituting a cryogenic thermal source and demonstrating <0.1% reflectance in 75-330 GHz spectral range, was reported in [7], alongside an accurate design model based on geometrical optics analysis. Considerable effort has been dedicated to adopting additive manufacturing techniques for millimeter-wave RAM structures, including 3D printed pyramidal absorber molds [8], and Hilbert curve impedance-matched structures [9]. Pyramidal tapers of various shapes represent the mainstream technology of broadband absorbers in microwave through infrared optical ranges [10,11].

Conventional open-foam and epoxy based broadband millimeter-wave RAM suffer from drawbacks such as high volume, weight, and low conformability, which affect the thermal budget of the cryogenic optical tubes and complicates absorber installation. An alternative electromagnetic absorber design approach is based on the use of thin multilayered engineered surfaces, conventionally referred to as planar metamaterials or metasurfaces. The use of the patterned conductive and resistive surfaces with controlled surface impedance, as well as a judicious choice of the dielectric interfaces enables robust and cost-effective solutions for millimeter-wave absorbers, as detailed in the following section.

This paper has a total of seven sections. In Section 2, a review of the planar electromagnetic absorbers is carried out, while the working principle of the new design is detailed in Section 3. Section 4 presents the device's modeling and its initial design. Preliminary fabrication and measurements of the absorber breadboards, aimed to evaluate the actual parameters of the materials and processes, are reported in Section 5. The refined recipe is used to fabricate the final device, and the respective results of its experimental characterization are presented in Section 6. The final conclusions are drawn in Section 7.

2. ABSORBING METASURFACES AT MICROWAVE- AND MILLIMETER-WAVE FREQUENCIES

A classic example of the absorbing surface design is the Salisbury screen, [12], described in detail in Section 3, where a resistive sheet is placed at a quarter-wavelength distance from a metallic reflector. Thinner structures can be realized using a high-impedance ground plane (HIGP) instead of a metallic reflector [13,14]. Another version of the device, the Dallenbach absorber, comprises a grounded quarter-wave slab of a lossy dielectric material [15]. Dielectric thickness specified in terms of the wavelength is a major cause of the narrowband performance of the conventional Salisbury and Dallenbach absorbers. The Jaumann absorber [13], which has multiple alternating layers of resistive sheets and low-density spacers, and the multilayer Dallenbach structures allow a significant bandwidth increase at the expense of an increased volume. Some hybrid broadband structures that combine the features of the 3D and planar multilayer absorbers have also been reported in microwave [16] and optical [17] frequency bands. HIGP-based structures appear to be inherently broadband.

Using patterned resistive grids instead of uniform sheets offers additional geometrical degrees of freedom in the design of thin broadband electromagnetic absorbers, [13,18]. Planar frequency selective surfaces (FSSs) with engineered surface impedance provide an effective way to reduce the thickness of absorbers. The respective design concept is known as the circuit-analog absorber (CAA) [19]. The resonant FSS layers could be either resistive or conductive stacked with uniform resistive sheets. Multi-octave bandwidth enhancement can be achieved in one of three ways: with a single-layer FSS with a double-periodic array of multiresonant dipoles or nested resonators [20], by stacking vertically single-resonant FSS sheets [21], or by combining both approaches [22]. However, the design of wideband resonant FSS absorbers has proven to be very involved, particularly with respect to the choice of the resonant elements and harmonic frequencies. Such absorbers also are inherently limited to a narrow angular range because of their polarization-dependent response at oblique incidence. Implementing intricate broadband FSS absorber designs in the terahertz range is technologically very challenging.

Using metasurfaces made of capacitive grids of subwavelength square patches, emulating a low-pass filter response, makes it possible to overcome the limitations of the resonant FSS structures in terms of the bandwidth and angle of incidence. The CAA design paradigm still applies. It has been theoretically shown that a capacitive CAA device, designed using four freestanding capacitive grids of resistive patches, could exhibit a 20 dB absorption within a ∼10 : 1 frequency range at normal incidence [19]. A large bandwidth with good angular coverage was demonstrated with a structure that has two lossy capacitive grids, a uniform resistive sheet, and five dielectric layers with low and high refractive indexes. The simulated structure exhibited a 20 dB absorption over a 7.5:1 bandwidth for up to a 45° angle of incidence for both TE and TM polarizations. Both structures reported in [19] feature a nearly optimum thickness for the given bandwidth, according to the Rozanov's criterion derived

in [23]; their performance, however, was only verified by simulations. A recent microwave metamaterial absorber structure in [24], designed with circuit modeling, has three layers of square resistive patches interspersed with dielectric layers. It demonstrates an ultra-wideband and wide-angle absorption response from 4.73 to 39.04 GHz (i.e., 8.25:1 band ratio) in simulations, which was partly confirmed by measurements within a reduced frequency band. The device thickness appeared to be a factor of 0.15 of the longest operating wavelength. A great variety of circuit-model designs of microwave absorbers aimed at achieving optimum performance in terms of the bandwidth, thickness, and reflectivity, have been reported in the literature, predominantly by simulations only. To the best of our knowledge, however, there has been only a rudimentary attempt to implement such structures from the millimeter wave through terahertz wave range, not to mention a lack of experimental demonstrations. It must be noted that such an implementation does not reduce to a simple scaling of the geometry, because of the specific behavior of the materials in the millimeter-wave range under specific operational conditions, as further discussed below.

The use of exotic metamaterial phenomena arising from concerted electric and magnetic polarizabilities of subwavelength scatterers allow even greater freedom in the design of absorbers in the millimeter through optical range. Although widely viewed as inherently narrowband and lossy, advanced dispersion-engineered metamaterial and metasurface structures feature increasingly broader performance. A 3D honeycomb-like metamaterial absorber reported in [25] demonstrated a 90% absorption bandwidth from 50 to 460 GHz (1:9.2 bandwidth ratio), as well as polarization and angle independence in a simulation. The concept of Huygens' metasurfaces, featuring inherent unidirectional scattering, has been employed to design a perfect metamaterial absorber [26], although at a single frequency. A conceptual multiband absorber for IR and optical bands proposed in [27] exploits the interference phenomena in stacked layers of epsilon-near-zero metamaterial and high-permittivity dielectric. It has been shown that bandwidth enhancement could be observed in plasmonic metamaterial absorbers [28].

In our opinion, despite the high volume of research on dispersion-engineered metamaterial absorbers, such devices remain relatively narrowband and lossy [29] for relevant discussion, and less practical from the points of view of design and manufacture, compared to the FSS and capacitive-grid absorbers. In addition, most of the research is based solely on simulations; very few frequency-downscaled prototypes have ever been manufactured and tested.

This paper presents the theory, design, fabrication, and experimental characterization of what we believe, to the best of our knowledge, is a novel millimeter-wave absorber based on a simple working principle: the use of a broadband magnetic mirror, rather than a metallic mirror, which can be built with dielectric layers and just one resistive sheet [30]. The higher the number of absorber layers, the larger the bandwidth. For the sake of demonstration, we set our requirement to those we use for CMB instruments, meaning a reflectivity at −20 dB level (i.e., 99% absorption) over a large frequency bandwidth (∼80 to 440 GHz; i.e., a 5:1 ratio), independence between S and P polarizations (perpendicular and orthogonal to the radiation plane of incidence), and high performance within a wide range of incidence angles (e.g., 0°–50°). We also aimed to develop a thin and flexible profile, compatible in terms of materials and manufacturing processes with the metal-mesh filters [31], flat lenses [32], and metamaterial half-wave plates [33], that we have developed in the past. The new absorber comprises four dielectric layers and one resistive mesh. The refractive indices of two layers were artificially synthesized by embedding subwavelength capacitive meshes within polypropylene. The device was designed using the same formalism we employed to develop an artificial magnetic conductor [30] based on the mesh filter technology. The new device, which had never been demonstrated before, successfully achieved these performance requirements.

3. MESH-ABSORBER SURFACE WORKING PRINCIPLE

Here, we describe the working principle of the new absorber, which implies a transition from the conventional means to absorb radiation using a perfect electric conductor as a backshort, to the idea to use a perfect magnetic conductor in its place.

A. Salisbury Screen

The simplest design for an effective absorbing surface is the Salisbury screen [12,13]. It consists of an absorbing sheet located at a quarter of the wavelength distance $\lambda_0/4$ from a metallic mirror, as shown in Fig. 1(a). The wavelength λ_0 defines the frequency ν_0 where the absorption is maximum. The radiation passing through the sheet will be in phase with that bouncing back from the mirror. This happens because the latter gains a phase factor π in the metal reflection and another factor π for the half-wavelength extra path back and forth, for a total of 2π. The standing wave created has its electric field maximum exactly where the absorbing sheet is. The surface impedance of the sheet is equal to the free-space impedance and provides unitary absorption and minimum reflection at the central frequency $\nu_0 = c/\lambda_0$, where c is the speed of light.

These structures can be easily modeled using transmission-line or propagation-matrix codes. In this work, we have chosen our central frequency to be $\nu_0 = 240$ GHz. The frequency dependent absorption and reflection coefficients for a Salisbury screen are shown in Fig. 2, curves labeled "a." The averaged absorption (and reflection) coefficients across a 5:1 bandwidth around ν_0 (i.e., from 80 GHz to 400 GHz), are, respectively, $A = 87.8\%$ and $R = -9.1$ dB. This is obtained by setting the absorber surface impedance equal to the free space impedance, $Z_{\text{abs}} = 377\ \Omega/\square$.

We note that if the absorbing sheet has a frequency-independent impedance, the equiphase condition also will be satisfied at higher frequencies, those for which the absorber-backshort distance is an odd multiple of their quarter wavelength [i.e., when $\lambda_0/4 = (2m+1)\lambda_m/4$, where $m = 0, 1, \ldots$]. The result is a periodic absorption (and reflection) behavior with maxima (and minima) at harmonic frequencies $\nu_1 = 3\nu_0$, $\nu_2 = 5\nu_0$, and so on.

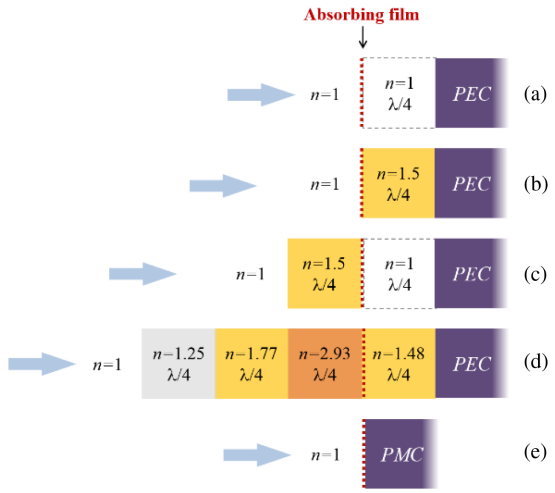

Fig. 1. Sketch of different types of absorbers based on an absorbing film: (a) Salisbury screen (air gap); (b) Salisbury screen on substrate; (c) Salisbury screen on substrate and air gap; (d) realization of a magnetic mirror absorber; and (e) ideal magnetic mirror-based absorber.

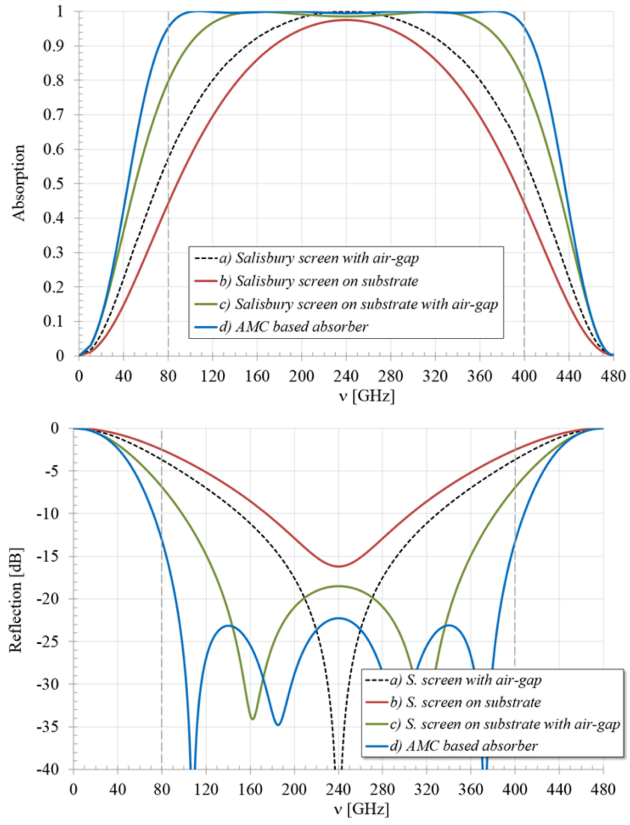

Fig. 2. Absorption and reflection coefficients versus frequency for the different absorbers: (a)–(d) sketched in Fig. 1.

B. Salisbury Screens on Substrates

The goal of our work is twofold: i) to design a robust absorbing device supported by dielectric substrates that could be manufactured using the mesh-filter technology; and 2) to obtain high absorption over very large bandwidths.

The first attempt would be to study an embedded version of the Salisbury screen. It could be made by replacing the $\lambda_0/4$ air gap with a quarter-wavelength dielectric layer ($\lambda_0/4\,n$) and by depositing the absorber on its external surface, as shown in Fig. 1(b). This would lead to a device much more robust than the previous one. However, by using polypropylene, for example, as a substrate (refractive index $n \cong 1.5$), the optimized design (with $Z_{abs} = 273\,\Omega/\square$) would decrease the average absorption within the 5:1 band down to $A = 80.9\%$ ($R = -7.2$ dB), as shown by the curves labeled "b" in Fig. 2. This is because some additional out-of-phase reflection is now added at the free-space to dielectric boundary, where the absorber is. Indeed, a mismatch from a low to high index implies a negative reflection coefficient.

We can look at a different configuration where the substrate and the absorbing film are now reversed compared to the incoming radiation direction; i.e., we keep the absorbing film at the same distance from the metal backshort but we reverse the position of its substrate, as shown in Fig. 1(c). The optimized absorption curve (obtained with $Z_{abs} \cong 213\,\Omega/\square$) changes dramatically and its 5:1 band average boosts up to $A = 96.8\%$ ($R = -15.0$ dB), as shown by the curves labeled "c" in Fig. 2. This is because some additional in-phase reflection is now added at the dielectric to free-space boundary (high to low index), where the absorber is. The effect we are describing is at the roots of the main idea of this work; i.e., forcing most of the radiation to be reflected in the phase where the absorbing surface is. This can be achieved by using a magnetic mirror, as described in the next section.

We note that the latter configuration, although showing good performance, would be difficult to manufacture because it would require a structure that could maintain the air-gap distance constant over large surfaces. It would be even more challenging to develop it if the absorbing surface is not meant to be flat.

C. AMC-Based Absorber

Magnetic mirrors, or artificial magnetic conductors (AMCs), are surfaces designed to mimic the behavior of the ideal perfect magnetic conductors (PMCs). These ideal materials reflect 100% of the incident radiation, they provide a null phase shift and can be modeled as surfaces exhibiting infinite impedance. This contrasts with normal perfect electric conductors (PECs), which provide a π phase shift and can be modeled with a null surface impedance.

As we have seen in the previous section, the quarter-wavelength air or dielectric gap is the main factor affecting the bandwidth and a natural way to improve absorption is to have in-phase reflection right at the absorber plane. By definition, the radiation reflected off a magnetic mirror is in phase with the incident one and an absorber located right on its surface should greatly increase its efficiency. This means that the maximum of the electric fields is no longer localized at a certain $\lambda_0/4$ distance from the mirror-backshort but is directly on its surface. This does not impose any geometrical constraint or frequency dependence to the system. Such an ideal system, sketched in Fig. 1(e), would absorb radiation at all frequencies; i.e., it would have an infinite bandwidth.

There are many ways to design magnetic mirrors (or AMCs). Here, we base our work on a device developed using the mesh-filter technology that led to multi-octave bandwidth operation [30]. The working principle of this magnetic mirror, part of the device sketched in Fig. 1(d), is based on the null phase shift obtained in the reflection occurring at a high-to-low index boundary. The higher the index difference, the higher the reflection coefficient. For this reason, a graded index section is used at the device input to drive the radiation adiabatically into a high index medium. A sudden jump into a lower index medium provides a high reflection coefficient with a null phase shift over large bandwidths. A backshort located at a quarter wavelength in that medium defines the central frequency of operation.

The broadband mesh-absorber presented here is made with a magnetic mirror similar to the one described above with an embedded absorber film located at the high-to-low index interface, as shown in Fig. 1(d).

4. MODELING AND INITIAL DESIGN

The absorber presented in this work is based on the mesh-filter technology. In this section, we briefly describe this technology and how we model the device and its initial design. Then, the details of the absorbing film will be discussed in Section 5.

A. Mesh-Filter Technology

The mesh absorber was manufactured using the processes developed for mesh-filters [31]. This has been employed not only to realize filters, used in many astronomical instruments operating at millimeter and sub-millimeter waves, but also to develop novel devices such as flat mesh lenses [32] and mesh half-wave plates [33]. The devices are manufactured by embedding metal grids within polypropylene layers, and by hot-pressing them all into a single homogenous polypropylene matrix where the metal grids remain suspended within it. In this specific application, the grids are not designed to interfere, like the devices mentioned above; instead, they are closed-packed to create the artificial dielectrics [34] required for the absorber's graded index medium.

A sketch of the ideal mesh-absorber made with homogeneous materials and its actual realization employing mesh-filter technology are shown, respectively, in Figs. 3(a) and 3(b). The ideal device requires four quarter-wavelength layers: the first three with increasing refractive indices ($n_1 = 1.25$, $n_2 = 1.77$, and $n_3 = 2.93$) and the last one with a low intermediate index ($n_4 = 1.48$). The absorbing film, with an optimized surface impedance $Z_{abs} \cong 103\ \Omega/\square$, is located between the third and the fourth layers. The metal backshort is at the end of the stack. The absorption curve is now very close to 1 across the 5:1 bandwidth around ν_0, as shown by the curves labeled "d" in Fig. 2, and its average value is boosted up to $A = 99.5\%$ ($R = -23$ dB).

The materials generally employed to build mesh-devices are: i) porous polytetrafluoroethylene (PTFE) ($n_{pPTFE} \cong 1.25$), used as anti-reflection (AR) coating; and ii) polypropylene ($n_{PP} \cong 1.48$), used as the substrate supporting the embedded metal grids. These two materials can be used respectively for the first and the fourth layer of the mesh-absorber, so that

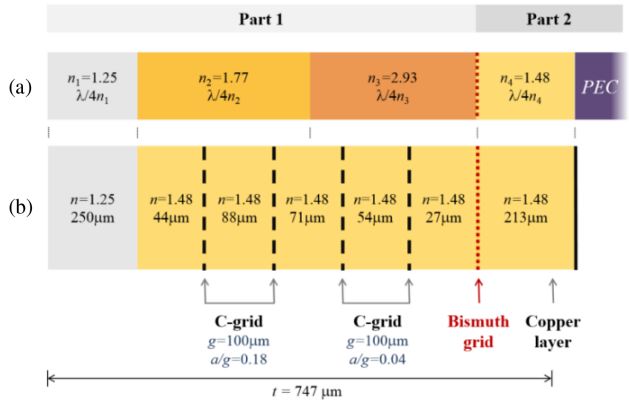

Fig. 3. (a) Sketch of the magnetic mirror absorber made with homogeneous materials and (b) sketch of the mesh-absorber realization using copper grids and the bismuth layer embedded into polypropylene.

$n_1 = n_{pPTFE}$ and $n_4 = n_{PP}$. However, the indices n_2 and n_3 can be artificially synthesized by embedding close-packed copper grids into polypropylene, following a method described elsewhere [34]. The two quarter-wavelength sections will require pairs of embedded capacitive grids; i.e., periodic square patches, with different filling factors. The capacitive grids have a period of $g = 100$ μm and this size allows the artificial media to be "seen" by the radiation as homogeneous dielectrics, with indices very close to n_2 and n_3, across a large bandwidth (0–500 GHz) [30].

The material used for the absorbing film is bismuth. The film will be required to have a specific pattern and surface impedance, which will be discussed in detail in Section 5. The metal backshort is realized with a 400 nm copper deposition.

The final device, apart from the AR coating layer, is completely made with polypropylene with the four capacitive grids, the absorber, and the backshort either embedded or deposited on it, as shown in Fig. 3(b). The total thickness of the device is ∼750 μm, which is equivalent to ∼0.6 λ and ∼0.2 λ, respectively, at the central and lowest operational frequencies.

B. Finite-Element Modeling

As mentioned in Section 3, the performance of the devices sketched in Fig. 1 have been computed using a propagation matrix code. In this case, the absorbing films were modeled as shunt admittances, the various layers as homogenous media, and the radiation assumed to be at normal incidence. The actual mesh-absorber device is made with homogeneous layers, but also with metamaterials that can be accurately simulated using finite-element analysis (FEA). We used Ansys HFSS commercial software [35] for our preliminary modeling, detailed design, and parameter retrieval of the final manufactured device.

The HFSS models consist of unit cells with periodic boundaries that mimic infinite arrays, as shown in Fig. 4. The boundaries are of the "master & slave" type to allow the simulation of radiation at any angle of incidence and for both types of polarizations (S or P). The porous PTFE and the polypropylene substrates are modeled as homogenous dielectric materials (the latter with a frequency dependent loss tangent), and the metal grids as thin copper patches with finite conductivity. The absorbers are modeled in two different ways: a) as homogeneous

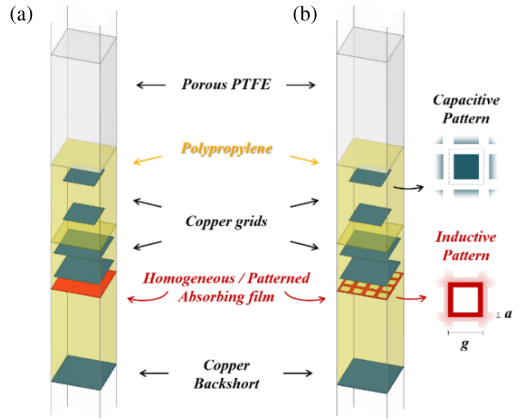

Fig. 4. Mesh-absorber HFSS models: (a) Homogeneous absorbing surface and (b) patterned (inductive) absorbing surface.

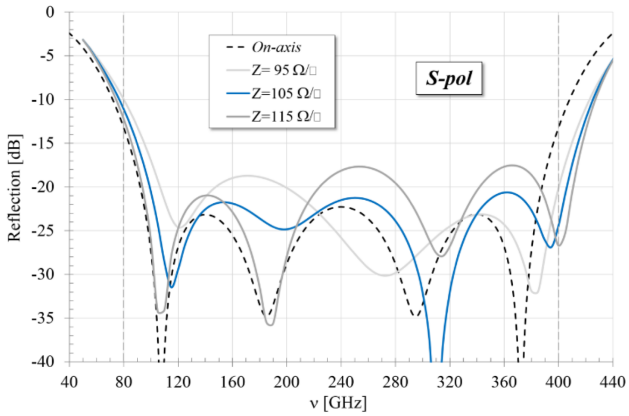

Fig. 5. S polarization reflection coefficient versus frequency for 22.5° incidence angle and different impedances for the absorber.

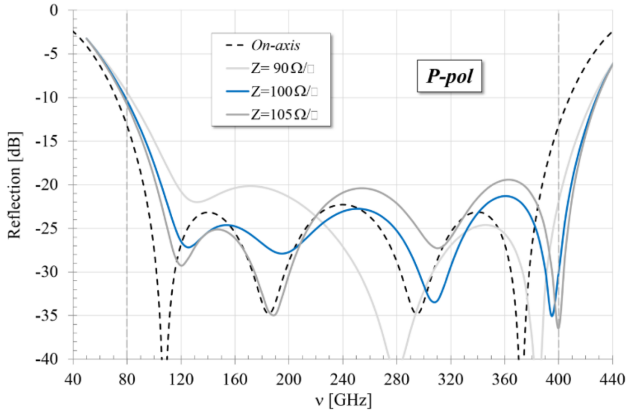

Fig. 6. P polarization reflection coefficient versus frequency for 22.5° incidence angle and different impedances for the absorber.

surfaces with associated impedance; and b) as patterned surfaces with associated surface impedance. The reason for using these two types of models will be clarified later.

In designing an absorbing device, in addition to low reflectivity and large bandwidth, there could also be requirements in terms of incidence angles. Depending on the application, the device might be required to work off-axis, or to maintain a high performance over a wide range of angles. In these cases, we expect the absorption to vary because the radiation will travel different path lengths through the absorber's layers. However, the absorber can be designed to have maximum performance at a specific angle θ, and this could correspond to the average angle within the range above. In our case, to prove the device's working principle we have chosen $\theta = 22.5$ deg, which corresponds to the reflection angle of our testing setups (see Section 6). We note that working off-axis implies the distinction between S and P polarizations, which means the absorber must be efficient in both configurations.

The initial design was simulated using a model of the type shown in Fig. 4(a); i.e., with a homogeneous absorbing surface between the third and the fourth layers. The surface impedance was varied in the range $95 - 115\ \Omega/\square$, the incidence angle was set to $\theta = 22.5$ deg, and both S and P polarization absorption coefficients were evaluated. The results of these simulations are shown in Figs. 5 and 6 for the S and P polarizations, respectively. The best averaged off-axis absorptions across the 5:1 bandwidth (80–400 GHz) were achieved by choosing these surface impedance values for the S and P polarizations: $Z_{\text{abs\_22.5\_}S} = 105\ \Omega/\square$ and $Z_{\text{abs\_22.5\_}P} = 100\ \Omega/\square$. The average of these values is close to the one obtained in the on-axis case; i.e., $Z_{\text{abs\_0}} \cong 103\ \Omega/\square$. By choosing the latter as an off-axis trade-off value, the averaged absorption appears to be almost polarization independent, at -21.6 dB level for both S and P polarizations. We note that the off-axis operation slightly shifts the operating band to higher frequencies, as shown in Figs. 5 and 6.

5. MANUFACTURE AND DESIGN FINE-TUNING

The manufacture of the mesh-absorber followed different steps: a) manufacture and tests of the graded index section (Part 1); b) research and development (R&D) on uniform resistive films; c) R&D on patterned resistive films; d) heat bonding test with a dummy absorber device; and e) manufacture of the backshort and the final assembly.

A. Part 1: Graded Index

The graded index part of the absorber (Part 1 in Fig. 3), was the first to be manufactured using standard mesh-filter processes. It consisted of three quarter-wavelength layers: The first was made with pPTFE (n_1), and the second and the third were made with polypropylene embedded capacitive meshes designed with their geometry and spacing to achieve the effective refractive indices of n_2 and n_3. The measured thickness of the assembly was close to the nominal value within the measurement error (~2 μm).

Transmission measurements were performed on-axis using the FTS to check the performance of this part of the absorber, as shown in Fig. 7. A finite-element model of Part 1 was built to compare its predictions with the measured data. The shape of the transmission curve of Part 1 is not relevant, but is useful to extract more accurate values of the various parameters. The measured data, up to 600 GHz, goes beyond the frequency range of the device. The transmission peak around 480 GHz is used to fit the data with higher accuracy. A four-parameter optimization of the finite-element model was run across a discrete number of frequency points to fit the measured data. The parameters were the pPTFE and polypropylene refractive indices and the

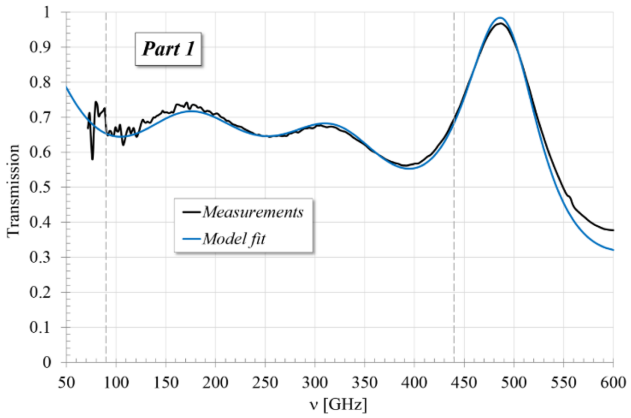

Fig. 7. Part 1 on-axis transmission measured and finite-element best fit model obtained by varying the pPTFE and PP refractive indices and the grid geometries.

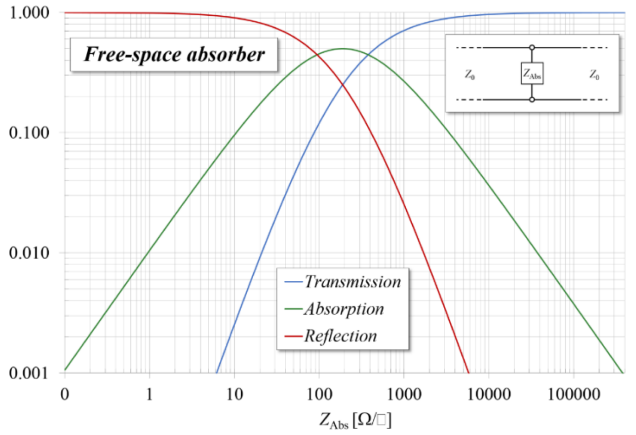

Fig. 8. Ideal free-space absorber transmission, absorption and reflection coefficients as a function of its surface impedance. The absorber is modeled as an infinite surface with no thickness.

a/g parameters of the two pairs of capacitive grids, as shown in Fig. 4. The overall thickness of Part 1 was set to the nominal one and the grid period ($g = 100$ μm) was not varied. The copper conductivity was assumed to have the standard value we use for these grids: $\sigma_{Cu} = 4 \times 10^7$ S/m. The fit procedure led to the following values: $n_{pPTFE} = 1.23$, $n_{PP} = 1.48$, $(a/g)_1 = 0.186$, and $(a/g)_2 = 0.045$. The refractive indices fall into the expected ranges of variability related to the bonding processes. The slightly higher fitted values of a/g, compared to the design values, imply overetching of the capacitive grids: The sides of the square patches ended up smaller by ∼1 μm in both pairs. The values of all the above parameters, either measured or estimated, will be used from now on to model this part of the device and to optimize other parts, as discussed in the following sections.

B. Homogeneous Absorbing Films

One way to realize a resistive sheet is to evaporate a thin film of metal on a polymer substrate. If the film thickness is well below the skin depth δ_S at all the frequencies of operation, the radiation going through the film will interact with the resistive layer and some of its power will be dissipated across it. For a given resistivity ρ and thickness t, the film surface impedance equals $Z_S = \rho/t$. If $t \ll \delta_S$, then the surface impedance can be considered constant with frequency.

In the case of an ideal freestanding resistive film, the transmission, absorption and reflection coefficients as a function of the surface impedance can be easily computed using a transmission line circuit. From these curves, reported in Fig. 8, we note that by measuring the transmission coefficient of an absorbing film, we can immediately infer its surface impedance.

One of the outcomes of the preliminary design is that the absorbing film of our device must have a surface impedance on the order of $Z_S \approx 103\ \Omega/\square$. Materials such as copper or gold cannot be used, because their high electrical conductivity would imply film thicknesses less than 1 nm. What is required is a metal with much lower conductivity (at least two orders of magnitudes below) that could also be evaporated on a polymer substrate and processed using the mesh-filter techniques. The conductivity of a thin film of evaporated bismuth depends on its thickness and varies typically in the range $\sigma_{Bi} \sim (0.35 \div 1.92) \times 10^5$ S/m

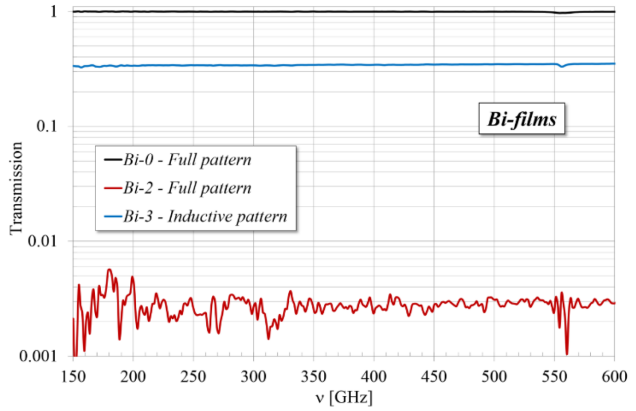

Fig. 9. Transmission measurements of the bismuth film samples.

for thicknesses $t = 14 \div 220$ nm [36]. Using these values as a starting point, the targeted $Z_S \sim 103\ \Omega/\square$ could be achieved with a bismuth film roughly 70 nm thick.

Before processing a specific absorbing film, some bismuth evaporation tests needed to be done on the polymer substrates normally used in mesh devices: Mylar and polypropylene. The bismuth deposition was processed via a thermal evaporation in a 10^{-6} mbar vacuum. Achieving reproducibility in the evaporation processes was one of the most critical factors. The first samples were tested in a transmission using an FTS test bed covering the frequency range of 150–600 GHz. Examples of these measurements are shown in Fig. 9. Having verified the very flat response with the frequency of the films, the samples manufactured subsequently were tested using a VNA test bed across a narrower frequency range; i.e., 160–260 GHz.

The first sample, Bi-1, was a 45 nm Bi film on a 0.9 μm thick Mylar substrate; the second, Bi-2, was a 450 nm Bi film on a 4 μm thick polypropylene. The Bi thickness was measured using a quartz crystal monitor calibrated using a surface profilometer (error of ±5%). These samples were useful to validate both the modeling tools and processing.

Bi-1 and Bi-2 samples showed constant transmissions on the order of $T_{Bi\text{-}1} \cong 0.252$ and $T_{Bi\text{-}2} \cong 0.003$, respectively. The curves in Fig. 8, although not including the small effects of

the thin substrates, can be used to infer the associated surface impedances with a good degree of accuracy (at a 1% level): $Z_{\text{Bi-1}} \sim 189\ \Omega/\square$ and $Z_{\text{Bi-2}} \sim 10\ \Omega/\square$. Simplified versions of the HFSS model shown in Fig. 4(a) have been used to infer the conductivity of bismuth. These models consisted of a dielectric substrate and a thin metal layer with variable conductivity. Optimization fits were run to match the transmission coefficients of the model and measured data, yielding the following conductivity values: $\sigma_{\text{Bi-1}} = 1.2 \times 10^5$ S/m and $\sigma_{\text{Bi-2}} = 2.2 \times 10^5$ S/m. These values are consistent (although outside their measured range) with those reported in [36].

C. Patterned Absorbing Films

A homogeneous absorbing film with the target impedance $Z_S \sim 103\ \Omega/\square$ could be, in principle, processed. However, the final device, as sketched in Fig. 3(b), requires the Bi-film to be sandwiched between polypropylene layers, and the associated heat-bonding process does not work in the presence of uniform metal layers. For this reason, the Bi-film must be patterned as an inductive grid; e.g., with square holes in it. This would allow the polypropylene layers on either side of the film to penetrate the sheet and bond during the hot-pressing process. We used an inductive pattern with a period $g = 25$ μm and the standard $a/g = 0.14$, as shown in Fig. 4(b).

For a given thickness, the surface impedance of a patterned layer of bismuth will be higher than for the uniform film, due to its dilution across the unit area. This means that the target surface impedance will be achieved with a thickness that is larger than the one estimated earlier (70 nm). The required thickness was estimated using another HFSS model (similar to the previous one but including a patterned bismuth layer) and it was $t \cong 180$ nm.

Again, before proceeding to the final film evaporation, the process above required some development. The inductive pattern was obtained using a lift-off process, rather than the standard etching process on a homogenous layer of bismuth. This was more suitable due to the materials, dimensions, and thicknesses involved. However, the lift-off process directly provided the final inductive pattern without the possibility to test first the uniform layer.

Two patterned film samples were processed, Bi-3 and Bi4, respectively, with a 90 nm and a 270 nm bismuth layer on 9 μm thick PP substrates. FTS and VNA transmission measurements provided averaged transmissions of $T_{\text{Bi-3}} \cong 0.340$ and $T_{\text{Bi-4}} \cong 0.050$, corresponding to the effective surface impedances of $Z_{\text{Bi-3}} \sim 263\ \Omega/\square$ and $Z_{\text{Bi-4}} \sim 54\ \Omega/\square$. Using the HFSS models and running optimizations to fit the data, it was possible to infer the values of the thin film conductivities and the results were: $\sigma_{\text{Bi-3}} = 1.4 \times 10^5$ S/m and $\sigma_{\text{Bi-4}} = 2.3 \times 10^5$ S/m.

Given the success with the previous processing, the final absorbing film with the targeted $Z_S \sim 103\ \Omega/\square$ now could be manufactured. The patterned sample Bi-5 had a 175 nm thick layer of bismuth on a 9 μm thick PP substrate. Its averaged transmission $T_{\text{Bi-5}} \cong 0.122$ implied an equivalent surface impedance $Z_{\text{Bi-5}} \sim 101\ \Omega/\square$ what was not far from the goal, and a film conductivity $\sigma_{\text{Bi-5}} = 1.9 \times 10^5$ S/m, which was close to what could be extrapolated from [36]; i.e., $\sigma_{\text{Bi}}(175\ \text{nm}) \cong 1.7 \times 10^5$ S/m. A summary of the properties of all the bismuth films is reported in Table 1.

Table 1. Bismuth Absorbing Film Characteristics

Film #	t [nm]	Pattern	T	Z_s Ω/□	σ_{HFSS} [S/m]
Bi-1	45	Full	0.252	189	1.2E+5
Bi-2	450	Full	0.003	10	2.2E+5
Bi-3	90	125/0.14	0.340	263	1.4E+5
Bi-4	270	125/0.14	0.050	54	2.3E+5
Bi-5	175	125/0.14	0.122	101	1.9E+5

D. Bonding Process Test with Dummy PP Layers and Absorbing Film

All the constituent parts of the mesh-absorber were ready to be assembled. The final process, required to be checked, was the bonding of the patterned bismuth film between PP layers, which had never been done before. For this purpose, the patterned Bi-3 sample was sandwiched and successfully hot-pressed between two layers of PP with thicknesses equal to those of the final device; i.e., 284 μm and 213 μm.

VNA transmission measurements of this "inefficient" dummy absorber were conducted to check for any potential variations of the surface impedance during the bonding process, as shown in Fig. 10. Two HFSS models were built to simulate the dummy sandwich with either the uniform or patterned resistive films. Both were used to fit the experimental data by varying the substrate's refractive index, equivalent surface impedance (first model), and conductivity of the bismuth thick pattern (second model). The optimization yielded almost indistinguishable transmission curves and the following values of the film parameters: $Z_{\text{Bi 3\_Dummy}} \sim 233\ \Omega/\square$ and $\sigma_{\text{Bi-3\_Dummy}} \sim 1.6 \times 10^5$ S/m. These results imply a reduction of ∼11% of the original impedance as a consequence of the bonding process.

E. Part 2 and the Final Assembly

The results provided by the dummy bonding implied a potential reduction of the surface impedance of the sample Bi-5 when bonded within the final device. An HFSS model of the complete

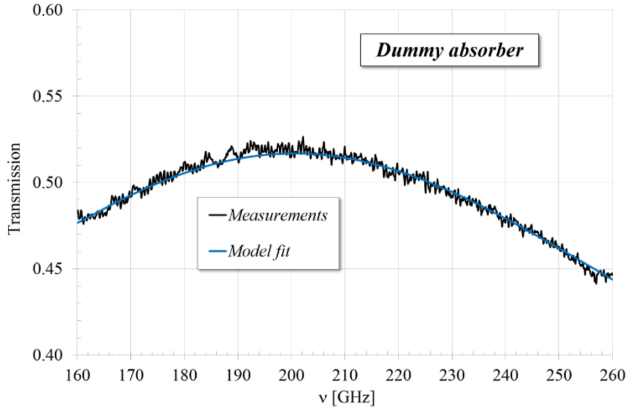

Fig. 10. Transmission measurements of the dummy absorber together with its best model fit obtained by varying the substrate refractive index and bismuth conductivity.

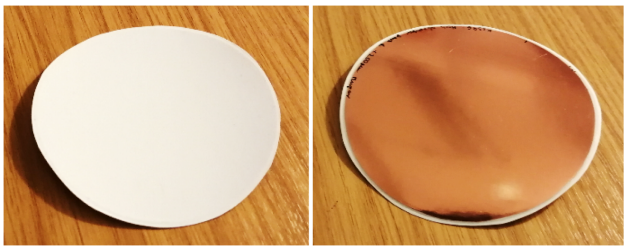

Fig. 11. Photographs of the mesh absorber taken from the AR-coating side (white) and from its copper backshort side. The device is mechanically flexible and has a diameter of 100 mm and a thickness of ~750 μm.

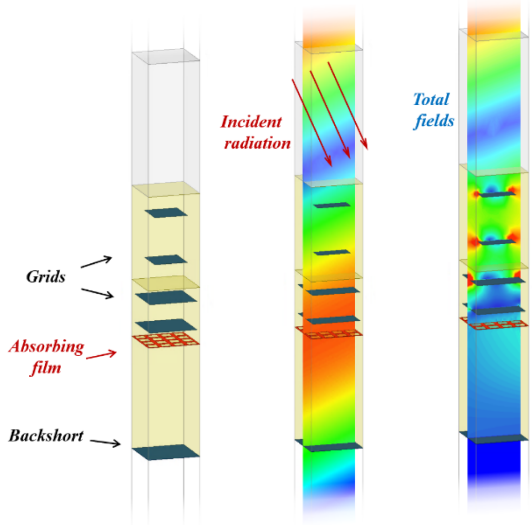

Fig. 12. Finite-element simulation showing the absorption of the electromagnetic field at 250 GHz, with light incident at 22.5° and both S and P polarizations present.

absorber, including the patterned Bi-5 film with the nominal ($Z_{\text{Bi-5}} \sim 103\ \Omega/\square$) and reduced ($Z_{\text{Bi-5\_red}} \sim 91\ \Omega/\square$) values of the surface impedance was run for each polarization. The overall absorption averaged over the 80–400 GHz band appeared to remain below −20 dB for both S and P polarizations, thus allowing us to proceed with the assembly of the final mesh-absorber.

The manufacturing process for Part 2 was straightforward, because this part consisted of bonded layers of PP with uniform copper evaporation on one side, as shown in Fig. 3(b). The whole device was eventually manufactured by stacking and hot-pressing Part 1, Bi-5, and Part 2. Photographs of the front and back sides of the final mesh-absorber are shown in Fig. 11. An example of the finite-element simulations of the mesh-absorber, run at 250 GHz, are shown in Fig. 12.

6. EXPERIMENTAL CHARACTERIZATION

Here, we briefly describe the experimental setups used for the various tests and the detailed characterization of the final mesh-absorber.

A. VNA and FTS Experimental Setups

The breadboard samples and the final device were tested using two different testbeds: a Fourier transform spectrometer of the Martin–Puplett type, operating in the 50–600 GHz frequency range by means of a cryogenically cooled bolometer detector, and a Rohde & Schwartz ZVA67 vector-network analyzer operating from 75 to 330 GHz by means of standalone frequency extenders. As mentioned earlier, the FTS was initially used to measure the transmission coefficients of the first Bi-samples and verify their broadband flat response. The VNA was then used to extract the surface impedances of the other Bi-samples over narrower frequency ranges and to quantify the Bi conductivity changes in the dummy absorber. The FTS was used for the transmission measurements of Part 1 and for the full-band reflection measurements of the final absorber. The relevant experimental setups have been described in detail elsewhere: the VNA transmission measurements in [37], the FTS transmission measurements in [33], and the FTS reflection measurements in [38].

We notice that the sample flatness proved to be a crucial factor for the data quality in the reflection measurements. In the tests, the absorber device was clamped in a holder and placed inside a mount behind an aperture. In the test, the holder was rotated about the optical axis and the small deviations of the received signal provided evidence of suitable flatness.

B. Absorber Tests and Results

The mesh absorber was tested with the FTS at a 22.5° incidence angle with both S and P polarizations. The measured data are reported in Figs. 13 and 14. A very good performance of the device across a wide frequency band is immediately evidenced for both polarizations. Quantitatively, the measured absorption coefficients averaged in the 80–400 GHz (a 5:1 bandwidth) frequency range, for both polarizations, were $A_{22.5\_S} = 99.2\%$ ($R_{22.5\_S} = -21.2$ dB) and $A_{22.5\_P} = 99.4\%$ ($R_{22.5\_P} = -22.0$ dB), respectively. These results meet the requirement that was set at the beginning; i.e., absorption to be ≥99% (reflection ≤ − 20 dB). Also, the differential absorption between S and P polarizations were very small, at the 0.2% level.

Although the design and development procedure successfully led to the desired performance, we have tried to fit the final data

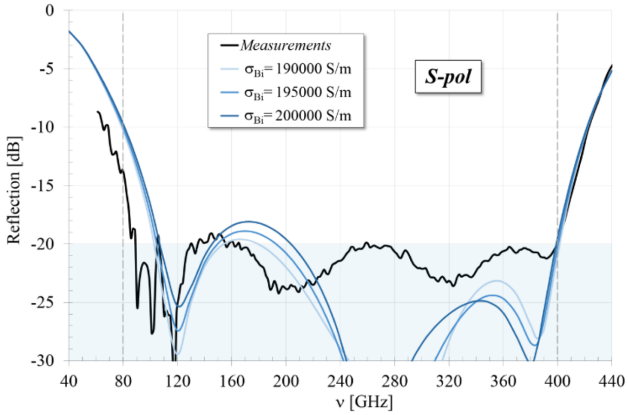

Fig. 13. Mesh-absorber simulated and measured reflection coefficient versus frequency for the S polarization at 22.5° incidence angle.

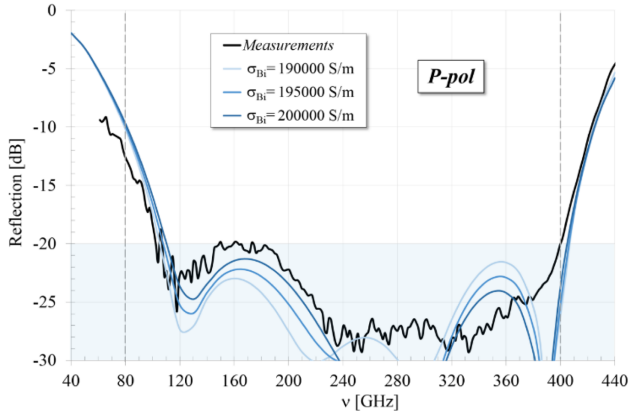

Fig. 14. Mesh-absorber simulated and measured reflection coefficient versus frequency for the P polarization at a 22.5° incidence angle.

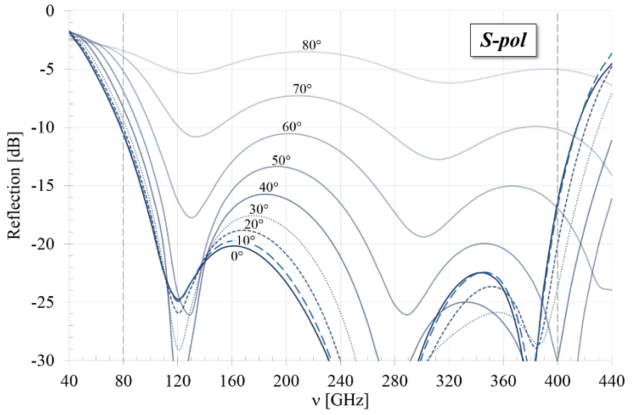

Fig. 15. Mesh-absorber simulated spectral response for different incidence angles for the S polarization.

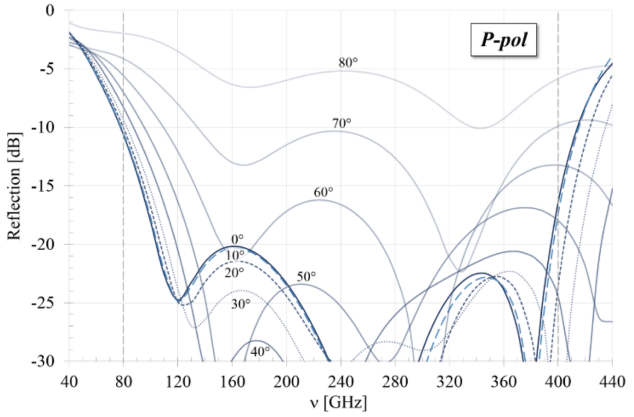

Fig. 16. Mesh-absorber simulated spectral response for different incidence angles for the P polarization.

with an HFSS model, as shown in Fig. 4(b). Within the many parameters required to run the model, some were identified and fixed previously: the copper conductivity, the device thickness (directly measured) and the capacitive grid geometries $(a/g)_{1,2}$ (extracted by testing Part 1). The remaining parameters, the PP and pPTFE refractive indices as well as the bismuth conductivity, could still change during the final bonding, and we let them vary in the final fit. Changes in n_{PTFE} provided negligible variations in the performance, whereas, as observed in the past [33], a systematic increase of n_{PP} shifted the overall curve toward the low frequencies. In addition, as learned by testing the dummy absorber, we also expected an increase of $\sigma_{\mathrm{Bi\text{-}5}}$. The models that better reproduced the measured data are shown in Figs. 13 and 14. The required values of the refractive indices were $n_{\mathrm{pPTFE}} = 1.23$ and $n_{\mathrm{PP}} = 1.51$. We reported the model results for three increasing values of the bismuth conductivity, starting from the initial one estimated before the bonding; i.e., $\sigma_{\mathrm{Bi\text{-}5}} = 1.9{-}2.0 \times 10^5$ S/m.

There is a good agreement between the simulations and data for both polarizations down to a −20 dB level. Below that, down to the noise floor of the FTS, at roughly −30 dB, there are variations, especially in the S polarization case. These variations are actually not important, because they are well below the requirement we set. In any case, we have tried to fit the data by going back and varying the parameters that were initially fixed, but we could not fit all the features. Our explanation is that the grids, when stacked together to manufacture the device, were not necessarily aligned. The capacitive grids were probably displaced (with the square patches not aligned as in Fig. 4) and rotated with respect to each other. An HFSS model with such arbitrary rotations cannot be built using periodic boundaries and the associated small changes in the performance could not be replicated. This observation suggests that future devices should be built with aligned grids.

Another important characteristic of these devices that was not investigated experimentally but simulated using the same models, is the dependence of the absorption on the angle of incidence. The results of the simulations are shown in Figs. 15 and 16 for the S and P polarizations. The parametric plots demonstrate the excellent performance of the mesh-absorber for large incidence angles. The absorption coefficient, averaged over the 80–400 GHz range and for both polarizations, is still above 97% at 50° ($A_{50\_S\&P} \geq 97\%$ and $R_{50\_S\&P} \leq -16$ dB) and above 87% at 70° ($A_{70\_S\&P} \geq 87\%$ and $R_{70\_S\&P} \leq -8.9$ dB). The same models also showed complete independence from the azimuthal angle.

7. CONCLUSIONS

We have presented the development of what we believe, to the best of our knowledge, is a novel type of broadband absorber based on mesh filter production processes. The manufacture of the first part of the device relied on the previous development of the mesh-based magnetic mirror. The second part required R&D for the evaporation of thin films of bismuth on polymers, lift-off processes for bismuth patterning, and testing of the bismuth film bonding within polypropylene. These activities were run side by side with finite-element modeling (HFSS) and experimental characterization (FTS and VNA test beds) that fed back evaluated surface impedances and conductivities of the bismuth films between the various processes. The final device was assembled and tested in reflection at a 22.5° incidence angle. The absorption coefficient, averaged across the 80–400 GHz

range (a 5:1 bandwidth), was $A_{22.5\_S} = 99.2\%$ for the S polarization, and $A_{22.5\_P} = 99.4\%$ for the P polarization, with just a 0.2% differential absorption between the two polarizations.

The simulations showed that the device can operate efficiently across a wide range of incidence angles, with absorption still above 97% at a 50° incidence and above 87% at a 70° incidence.

On the thermo-mechanical side the device is: thin (750 μm; i.e. $0.6\lambda_0$ at the central frequency of 240 GHz, or 0.2λ at the lowest frequency of 80 GHz), very light (8 g for a 100 mm diameter), flexible (applicable on curved surfaces), machinable (can be cut to any shape), and suitable for cryogenic temperatures (taking into account the change of the bismuth conductivity with temperature).

We note that the broadband mesh-absorber performance stems from the magnetic mirror design reported in [30]. By keeping the same number of layers and by tuning the design parameters, the absorption can in principle be pushed at any level at the expense of a reduced bandwidth. In addition, by increasing the number of layers of the graded index section (Part 1), it is possible to achieve much larger bandwidths. For example, a five-layer device with just one more layer than the reported absorber, can achieve similar performance across a relative bandwidth of 8:1. The device also exhibits absorption at higher harmonics, although its efficiency will be limited by the period of the metal grids.

Funding. Science and Technology Facilities Council (ST/N000706/1).

Acknowledgment. The authors would like to thank Dr. Matteo Ruggeri for his help during the modeling and data analysis phase.

Disclosures. The authors declare no conflicts of interest.

Data availability. Data underlying the results presented in this paper are not publicly available at this time but may be obtained from the authors upon reasonable request.

REFERENCES

1. L. Lamagna, J. E. Gudmundsson, H. Imada, *et al.*, "The optical design of the LiteBIRD middle and high frequency telescope," Proc. SPIE **11443**, 1144370 (2021).
2. Z. Xu, G. E. Chesmore, S. Adachi, A. M. Ali, A. Bazarko, G. Coppi, M. Devlin, T. Devlin, S. R. Dicker, P. A. Gallardo, and J. E. Golec, "The Simons observatory: metamaterial microwave absorber and its cryogenic applications," Appl. Opt. **60**, 864–874 (2021).
3. T. O. Klaassen, M. C. Diez, J. H. Blok, A. Drunk, K. J. Wildeman, and G. Jakob, "Optical characterization of absorbing coatings for submillimeter radiation," in *Twelfth International Symposium on Space Terahertz Technology* (2001), p. 400.
4. R. Wylde, "Space qualified tessellating Terahertz RAMs for the 50 to 1000 GHz region and beyond," Thomas Keating Ltd., http://www.terahertz.co.uk/index.php?option=com_content&view=article&id=145&Itemid=448.
5. Henkel Corporation, "Technical Data Sheet LOCTITE STYCAST 2850FT," (2016), https://www.henkel-adhesives.com/us/en/product/potting-compounds/loctite_stycast_2850ft.html.
6. K. Rostem, E. Cimpoiasu, K. R. Helson, A. P. Klassen, and E. J. Wollack, "Specific heat of epoxies and mixtures containing silica, carbon lamp black, and graphite," Cryogenics **118**, 103329 (2021).
7. D. T. Chuss, K. Rostem, E. J. Wollack, L. Berman, F. Colazo, M. DeGeorge, K. R. Helson, and M. Sagliocca, "A thermal cryogenic source for detector array characterization," Rev. Sci. Instrum. **88**, 104501 (2017).
8. S. Adachi, M. Hattori, F. Kanno, K. Kiuchi, T. Okada, and O. Tajima, "Production method of millimeter-wave absorber with 3D-printed mold," Rev. Sci. Instrum. **91**, 016103 (2020).
9. M. Petroff, J. Appel, K. Rostem, C. L. Bennett, J. Eimer, T. Marriage, J. Ramirez, and E. J. Wollack, "A 3D-printed broadband millimeter wave absorber," Rev. Sci. Instrum. **90**, 024701 (2019).
10. E. J. Wollack, A. M. Datesman, C. A. Jhabvala, K. H. Miller, and M. A. Quijada, "A broadband micro-machined far-infrared absorber," Rev. Sci. Instrum. **87**, 054701 (2016).
11. E. J. Wollack, R. E. Kinzer, and S. A. Rinehart, "A cryogenic infrared calibration target," Rev. Sci. Instrum. **85**, 044707 (2014).
12. W. Salisbury, "Absorbent body of electromagnetic waves," U.S. patent 2,599,944 (10 June 1952).
13. B. A. Munk, *Frequency Selective Surfaces: Theory and Design* (Wiley, 2000).
14. F. Costa and A. Monorchio, "Electromagnetic absorbers based on high-impedance surfaces: from ultra-narrowband to ultra-wideband absorption," Adv. Electromagn. **1**, 7–12 (2012).
15. P. Saville, "Optimisation of Dallenbach layers using real materials," Technical memorandum DRDC Atlantic TM 2007-012 (Defence R&D Canada, 2007).
16. X. Lleshi, R. Grelot, T. Q. V. Hoang, B. Loiseaux, and D. Lippens, "Wideband metal-dielectric multilayer microwave absorber based on a single step FDM process," in *49th European Microwave Conference* (2019), pp. 679–681.
17. M. Song, H. Yu, C. Hu, M. Pu, Z. Zhang, J. Luo, and X. Luo, "Conversion of broadband energy to narrowband emission through double-sided metamaterials," Opt. Express **21**, 32207–32216 (2013).
18. F. Costa, A. Kazemzadeh, S. Genovesi, and A. Monorchio, "Electromagnetic Absorbers based on Frequency Selective Surfaces," in *Forum for Electromagnetic Research Methods and Application Technologies (FERMAT)* (2016).
19. D. Sjoberg, "Analysis of wave propagation in stratified structures using circuit analogues, with application to electromagnetic absorbers," Eur. J. Phys. **29**, 721–734 (2008).
20. B. X. Wang, Y. He, P. Lou, W. Q. Huang, and F. Pi, "Penta-band terahertz light absorber using five localized resonance responses of three patterned resonators," Results Phys. **16**, 102930 (2020).
21. L. Li and Z. Lv, "Ultra-wideband polarization-insensitive and wide-angle thin absorber based on resistive metasurfaces with three resonant modes," J. Appl. Phys. **122**, 055104 (2017).
22. J. Chen, Y. Shang, and C. Liao, "Double-layer circuit analog absorbers based on resistor-loaded square-loop arrays," IEEE Antennas Wireless Propag. Lett. **17**, 591–595 (2018).
23. K. N. Rozanov, "Ultimate thickness to bandwidth ratio of radar absorbers," IEEE Trans. Antennas Propag. **48**, 1230–1234 (2000).
24. P. Chen, X. Kong, J. Han, W. Wang, K. Han, H. Ma, L. Zhao, and X. Shen, "Wide-angle ultra-broadband metamaterial absorber with polarization-insensitive characteristics," Chin. Phys. Lett. **38**, 027801 (2021).
25. A. Vahidi, H. Rajabalipanah, A. Abdolali, and A. Cheldavi, "A honeycomb-like three-dimensional metamaterial absorber via super-wideband and wide-angle performances at millimeter wave and low THz frequencies," Appl. Phys. A **124**, 337 (2018).
26. J. L. Araque-Quijano, J. P. del Risco, M. A. Londoño, A. Sayanskiy, S. B. Glybovski, and J. D. Baena, "Huygens' metasurfaces covering from waveplates to perfect absorbers," in *International Conference on Electromagnetics in Advanced Applications (ICEAA)* (2018), pp. 511–514.
27. L. La Spada and L. Vegni, "Metamaterial-based wideband electromagnetic wave absorber," Opt. Express **24**, 5763–5772 (2016).
28. Y. Pang, J. Wang, H. Ma, M. Feng, Y. Li, Z. Xu, S. Xia, and S. Qu, "Spatial k-dispersion engineering of spoof surface plasmon polaritons for customized absorption," Sci. Rep. **6**, 29429 (2016).
29. P. Yu, L. V. Besteiro, Y. Huang, J. Wu, L. Fu, H. H. Tan, C. Jagadish, G. P. Wiederrecht, A. O. Govorov, and Z. Wang, "Broadband metamaterial absorbers," Adv. Opt. Mater. **7**, 1800995 (2018).
30. G. Pisano, P. A. R. Ade, and C. Tucker, "Experimental realization of an achromatic magnetic mirror based on metamaterials," Appl. Opt. **55**, 4814–4819 (2016).

31. G. Pisano, C. Tucker, P. A. R. Ade, P. Moseley, and M. W. Ng, "Metal mesh based metamaterials for millimetre wave and THz astronomy applications," in *2015 8th UK, Europe, China Millimeter Waves and THz Technology Workshop* (2015), pp. 1–4.
32. G. Pisano, A. Shitvov, P. Moseley, C. Tucker, G. Savini, and P. Ade, "Development of large-diameter flat mesh-lenses for millimetre wave instrumentation," Proc. SPIE **10708**, 107080D (2018).
33. G. Pisano, A. Ritacco, A. Monfardini, C. Tucker, P. A. R. Ade, A. Shitvov, A. Benoit, M. Calvo, A. Catalano, J. Goupy, S. Leclercq, J. Macias-Perez, A. Andrianasolo, and N. Ponthieu, "Development and application of metamaterial-based half-wave plates for the NIKA and NIKA2 polarimeters," Astron. Astrophys. **658**, A24 (2022).
34. J. Zhang, P. A. R. Ade, P. Mauskopf, L. Moncelsi, G. Savini, and N. Whitehouse, "New artificial dielectric metamaterial and itsapplication as a THz anti-reflection coating," Appl. Opt. **48**, 6635–6642 (2009).
35. Ansys HFSS, "Best-in-class high frequency structure simulation software," https://www.ansys.com/products/electronics/ansys-hfss.
36. C. Yang, "*A Study of Electrical Properties in Bismuth Thin Films*," University of Florida (2008).
37. G. Pisano, M. W. Ng, V. Haynes, and B. Maffei, "A broadband metal-mesh half-wave plate for millimetre wave linear polarisation rotation," Prog. Electromagn. Res. M **25**, 101–114 (2012).
38. G. Pisano, B. Maffei, P. A. R. Ade, P. de Bernardis, P. De Maagt, B. Ellison, M. Henry, M. W. Ng, B. Schortt, and C. Tucker, "Multi-octave metamaterial reflective half-wave plate for millimeter and sub-millimeter wave applications," Appl. Opt. **55**, 10255–10262 (2016).